Medical Engineering and Physics 105 (2022) 103814

Contents lists available at ScienceDirect

Medical Engineering and Physics

journal homepage: www.elsevier.com/locate/medengphy

Patient-specific computational haemodynamics associated with the surgical creation of an arteriovenous fistula

George Hyde-Linaker [a], Pauline Hall Barrientos [b], Sokratis Stoumpos [c,d], David Brian Kingsmore [c], Asimina Kazakidi [a,*]

[a] Department of Biomedical Engineering, University of Strathclyde, Glasgow, UK
[b] Image Centre of Excellence, Queen Elizabeth University Hospital, Glasgow, UK
[c] Renal and Transplant Unit, Queen Elizabeth University Hospital, Glasgow, UK
[d] Institute of Cardiovascular and Medical Sciences, BHF Glasgow Cardiovascular Research Centre, University of Glasgow, Glasgow G12 8TA, UK

ARTICLE INFO

Keywords:
Arteriovenous fistulae
Vascular access
Haemodynamics
Chronic kidney disease
Computational fluid dynamics

ABSTRACT

Despite arteriovenous fistulae (AVF) being the preferred vascular access for haemodialysis, high primary failure rates (30-70%) and low one-year patency rates (40-70%) hamper their use. Furthermore, AVF creation has been associated with haemodynamic changes causing maladaptive cardiac remodelling leading to cardiovascular (CV) complications. In this study, we present a new workflow for characterising the haemodynamic profile prior to and following surgical creation of a successful left radiocephalic AVF in a 20-year-old end-stage kidney disease patient. The reconstructed vasculature was generated using multiple ferumoxytol-enhanced magnetic resonance angiography (FeMRA) datasets. Computational fluid dynamics (CFD) simulations utilising a scale-resolving turbulence model were completed to investigate the changes in the proximal haemodynamics following AVF creation, in addition to the post-AVF juxta-anastomosis flow patterns, which is impractical to obtain *in-vivo*. Following AVF creation, a significant 2-3-fold increase in blood flow rate was induced downstream of the left subclavian artery. This was validated through comparison with post-AVF patient-specific phase-contrast data. Proximal to the anastomosis, the increased flow rate yielded an increase in time-averaged wall shear stress (WSS), which is a key marker of adaptive vascular remodelling. In the juxta-anastomosis region, the success of the AVF was discussed with respect to the National Kidney Foundation's vascular access guidelines, where the patient-specific AVF met the flow rate and geometry criterion. The AVF venous diameter exceeded 6mm and the venous flow rate surpassed 600mL/min. This workflow may potentially be significant clinically when applied to multi-patient cohorts, with population-wide patient-specific conclusions being ascertained for the haemodynamic assessment of AVFs and improved surgical planning.

1. Introduction

In 2017, the global prevalence of chronic kidney disease (CKD) was 9.1%, which is roughly 700 million cases [1]. Patients with CKD experience a gradual decline in renal function to the extent that renal replacement therapy (RRT) is required for survival in end-stage kidney disease (ESKD). Over 85% of the global ESKD population is haemodialysis (HD) dependent [2], requiring a reliable access to the systemic circulation to achieve mechanical blood filtering and replace the kidney function. The preferred vascular access for ESKD patients is an arteriovenous fistula (AVF), a native vessel segment created by surgically joining a vein and an artery, commonly in the patient's non-dominant arm [3]. Creation of an AVF establishes a shunt from the high pressure, low capacitance arterial system, to the low pressure, high capacitance venous system [4], causing an increase in the arterial diameter and the 'arterialisation' (thickening and increased elasticity) of the vein. This process takes approximately 6-8 weeks [5] and, when successful, permits consistently high blood flow rates in excess of 600mL/min [6] whilst providing a durable vascular access for delivery of efficient and repeatable dialysis. The 6-week arterialisation period and 600mL/min minima flow rate fall under the successful AVF 'rule of six' criterion detailed in vascular guidelines [6]. In addition to flow rate, the AVF venous diameter should exceed 6mm and the AVF should have a depth from the skin surface no greater than 0.6cm.

* Corresponding author,
E-mail address: asimina.kazakidi@strath.ac.uk (A. Kazakidi).

https://doi.org/10.1016/j.medengphy.2022.103814
Received 9 November 2021; Received in revised form 3 May 2022; Accepted 4 May 2022
Available online 6 May 2022

A major problem with AVFs is the high frequency of primary failure as a result of either poor maturation or early thrombosis. As such, vascular access dysfunction is one of the leading causes of morbidity and mortality among ESKD patients [7,8]. Neointimal hyperplasia (NH) and inadequate outward venous remodelling are the two leading causes of AVF failure [9]. However, the exact mechanisms underlying these processes remain mostly unknown, highlighting the need for exploring further the haemodynamic environment caused by vascular access surgery [10–12]. Moreover, it has been reported that the successful creation of AVF may result in cardiac failure due to the marked increase in cardiac output over time [13]. The dual influence of increased cardiac output and reduced systemic vascular resistance post-AVF creation is an area of limited prior research. In this work, we aim to investigate these changes in a 20-year-old ESKD patient by combining novel vascular imaging (through ferumoxytol-enhanced magnetic resonance angiography, FeMRA) with high-fidelity computational fluid dynamics (CFD) analysis of the entire proximal vasculature to the arteriovenous fistula. This patient received a radiocephalic AVF, which is the clinically preferred AVF location [14].

CFD is a useful tool for assessing patient-specific haemodynamic predictors of AVF success or failure [15] beyond the traditional demographic, clinical and biological factors. This is due to the haemodynamics and wall shear stress (WSS) influencing the AVF environment being difficult to measure *in-vivo*. The use of CFD has been demonstrated in prior studies [16–18], which have described AVF flow characteristics in addition to proposing the conditions associated with luminal reduction. These sites are zones of low and oscillatory shear stress. CFD allows a wide range of calculations into such haemodynamic metrics [19–23]. This is key for assessing regions of patient-specific anatomical characteristics that are susceptible to abnormal WSS distributions and disturbed flow [24–26].

Here, we present a new framework for generating 3D reconstructions of the arterial vasculature, pre- and post-AVF creation. The reconstructions presented are based on ferumoxytol-enhanced magnetic resonance angiography (FeMRA) data. Ferumoxytol is a superparamagnetic iron oxide nanoparticle preparation, developed firstly as a contrast agent in 2000 [27]. The use of FeMRA avoids the risks that historic contrast-enhanced methods pose in ESKD patients. For example, gadolinium-based contrast agents (GBCAs) are linked with a risk of nephrogenic systemic fibrosis in ESKD. In this study, the haemodynamics of the 3D arterial reconstructions generated from multiple FeMRA scans were simulated using an established finite-volume implementation in Simcenter STAR-CCM+ (Siemens Industries Digital Software). A Scale-Resolving Hybrid (SRH) turbulence model was utilised to capture the potentially transitional-flow in the AVF. The use of CFD with FeMRA in this study demonstrates the potential for more thorough explanation of the complexities behind AVF maturation, NH, and cardiovascular impact. The aims of this study were to analyse WSS distributions at the peri-anastomotic region, the velocity profile in the proximal artery and venous outflow segments, and to elucidate haemodynamic changes in the proximal vasculature to the AVF (from the ascending aorta to the radial artery). Prior AVF CFD studies concentrated primarily on localised AVF haemodynamics, neglecting the consequences of increased cardiac output on the proximal vasculature to the AVF. The novelty of this study lies in elucidating the haemodynamics in this region, in addition to being the first study according to our knowledge that couples FeMRA with CFD in a workflow.

2. Materials and methods

In this research, we completed CFD investigations of two domains (pre- and post-AVF) that were each generated from three sets of FeMRA-obtained DICOM stacks (chest, upper arm, and lower arm). The pre-operative simulated vasculature extends from the ascending aorta to the radial artery, while the post-surgical reconstruction commences at the ascending aorta and terminates distally to the 'draining' vessels of the patient's 'end-to-side' radiocephalic AVF. Fig. 1 displays a simplified schematic of the centrelines within the computational domains used in the pre- and post-AVF simulations, along with the applied boundary conditions. In order to generate the pre-operative and post-surgery computational domains, each of the DICOM stacks were segmented, reconstructed, and then combined using a Boolean unification workflow in Meshmixer (Autodesk Meshmixer). These domains were then meshed and numerically modelled (Fig. 2).

2.1. Ferumoxytol-enhanced magnetic resonance angiography

Due to the differing scales of the vasculature in this study, three separate scans for the chest, left upper arm, and left lower arm were acquired (Fig. 2). This is due to the varying resolutions required when scanning smaller vessels as opposed to larger ones (Supplementary Material). The scans of the patient were performed before surgery and six weeks after AVF creation on a 3.0T Prisma MRI scanner (Magnetom, Siemens Medical Solutions) with local phased-array imaging coils using a standardised protocol similar to that of standard MRA studies with GBCAs. The patient was imaged in the supine position [27].

2.2. Generation of computational domain

Volume renderings of each DICOM stack were initially generated in order to visualise the vessels of interest. The key areas to assess visually were the common bifurcations between the three FeMRA scans of each visit, these being (i) the body and upper arm scans, and (ii) the upper arm and lower arm scans (Fig. 2). The two respective regions selected were the deep brachial artery bifurcation and the radial-ulnar bifurcation. These anatomical landmarks were used to align and unite the geometries and to create a single domain from the three DICOM stacks. Following this, each unified stack was segmented and reconstructed 'semi-automatically' using the open-source ITK-SNAP algorithms (www.itksnap.org). This involved manual editing following automatic segmentations that used a common threshold ratio [28]. These unstructured surface meshes of the reconstructions were exported into Meshmixer and manipulated so that the common areas (the deep brachial artery bifurcation and the radial-ulnar bifurcation) overlapped (Fig. 2). The daughter bifurcation vessels between scans were made colinear (Supplementary Material). The geometries were then combined using a 'Boolean Union' function in Meshmixer (Supplementary Material), with overlapping areas being smoothed to preserve the dimensions of the geometry whilst ensuring that the transition from one reconstruction to the other was valid anatomically. The dimensions of the STL surface mesh were compared to the initial DICOM files at various intervals for verification. The open-source 'Hole Filler' tool in OpenFlipper (RWTH Aachen), a framework for processing geometric data, was then used for resolving any areas of missing elements. Following this, the mesh was iteratively refined and 'smoothed' in OpenFlipper to ensure the mesh quality was sufficient at each bifurcation. The centrelines of the domain were subsequently computed utilising the VMTK libraries (http://www.vmtk.org) before clipping the inlet and outlets of the domain, normal to the vessel centreline, in Paraview (http://www.paraview.org). The domain was clipped normally at distances of 0.5D (inlet) and 1.5D (outlet) in a similar manner to prior studies [25], where D is the diameter of each respective patch. This approach mitigates potential boundary effects. Finally, the clipped inlet and outlet boundaries of the geometry were closed normal to the centreline in STAR-CCM+ in order to define the boundaries and volume of the domains (Fig. 3).

2.3. Hybrid mesh generation

A hybrid mesh with prism layers and polyhedral elements was used for discretising the computational domain (Supplementary Material). Polyhedral meshes contain approximately five times fewer cells than a

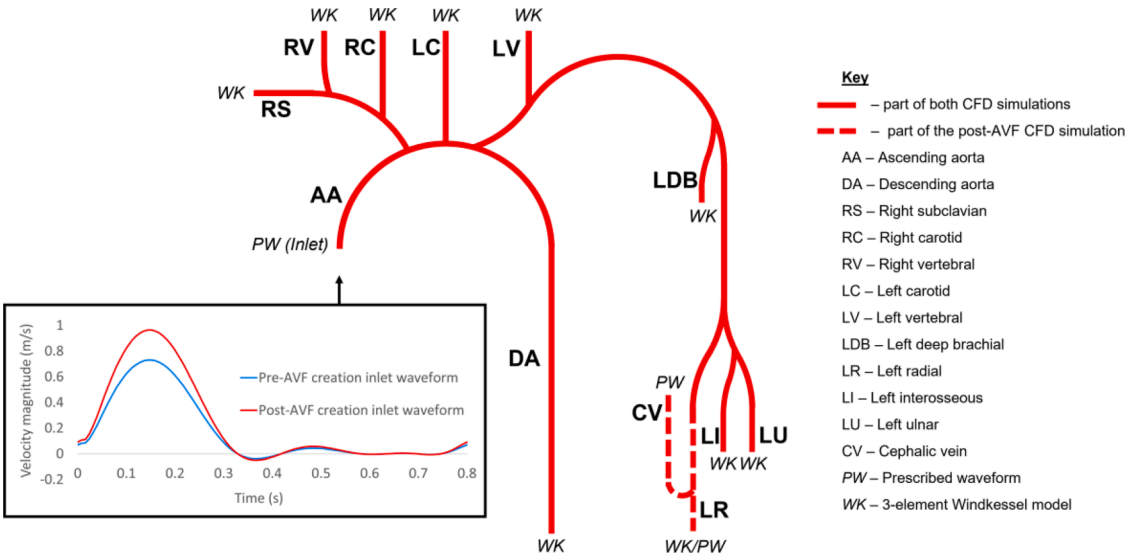

Figure 1. Simplified schematic of the vessels and boundary conditions of the computational domains used in the pre- and post-AVF simulations, where the solid line represents the common vessels in both domains and the dashed line represents vessels only in the post-AVF simulation. Three-element Windkessel models were used for the majority of outlets (in both simulations), the only exceptions being the cephalic vein and radial artery in the post-AVF simulation (which used prescribed outflows). The inlet velocity waveforms are displayed in the inset (where the blue waveform is the pre-AVF inlet, and the red waveform is the post-AVF inlet). (For interpretation of the references to color in this figure legend, the reader is referred to the web version of this article.)

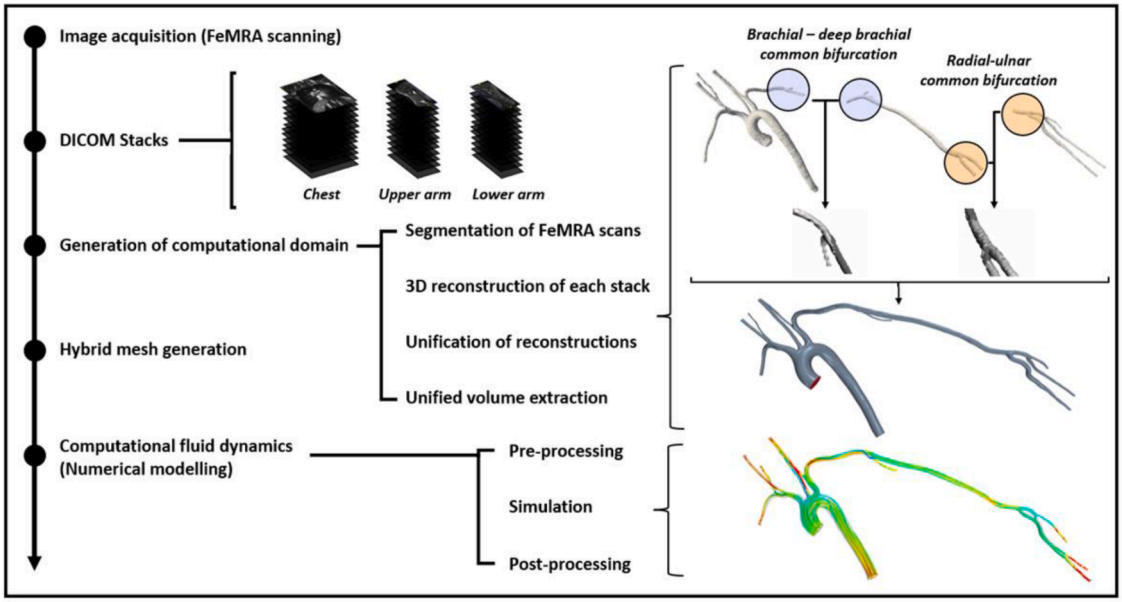

Figure 2. Framework used for the segmentation, reconstruction, geometry unification and volume extraction of the patient-specific geometry based on ferumoxytol-enhanced magnetic resonance angiography (FeMRA) multi-stack images and subsequent CFD analysis.

comparable tetrahedral mesh and are less sensitive to stretching. Prism layers were incorporated to reduce numerical diffusion adjacent to the wall and capture viscous effects. The height of the first prism layer, y, was calculated assuming a y+ value of 1 [25], given by:

$$y+ = \frac{\rho \cdot u_T \cdot y}{\mu} \tag{1}$$

where y+ is a dimensionless distance for describing the mesh density adjacent to domain walls, ρ is the fluid density, u_T is the friction velocity, y is the height of the first prism layer, and μ is the dynamic viscosity of the fluid.

Following the calculation of the initial prism layer height, a mesh independence study was completed for the pre-AVF case. The number of prism layers and cell base size was varied, whilst the prism layer total thickness was kept constant. The most suitable mesh had 8 prism layers and base size of 3.8E-4m, resulting in a hybrid mesh with 3776730 elements and a maximum y+ value of 0.36. The mean grid convergence index (GCI) [29] at 16 locations in the vasculature was computed as 0.99, which was deemed appropriate. This same mesh specification was applied for the post-AVF case. The mesh characteristics for each case were validated for the SRH model by computation of the maximum wall y+, and the Taylor Micro-, and Kolmogorov length scales (Supplementary Material), which are measures of turbulent flow structures that infer the required mesh resolution of the domain.

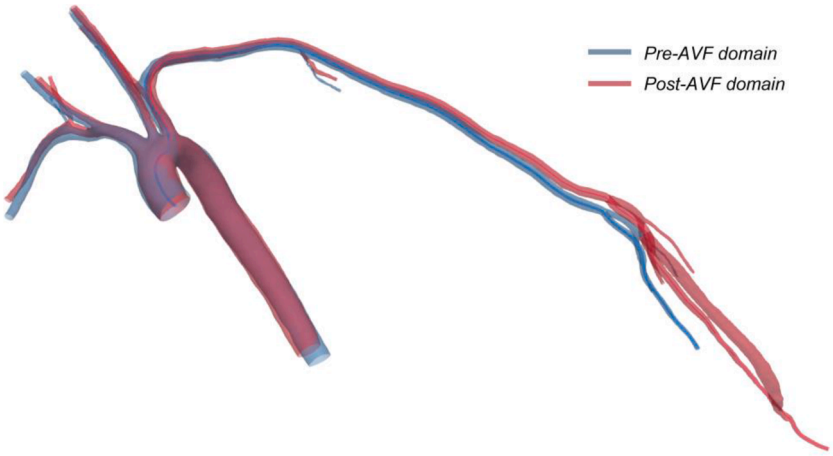

Figure 3. Pre- (blue) and post-AVF (red) domains and centerlines. (For interpretation of the references to color in this figure legend, the reader is referred to the web version of this article.)

2.4. Numerical modelling

2.4.1. Scale-resolving hybrid turbulence model

The SRH turbulence model (STAR-CCM+, Supplementary Material) is a hybrid RANS-LES (Reynolds-Averaged Navier-Stokes, Large Eddy Simulation) model which permits the computation of unsteady large-scale turbulence structures whilst having a computational expense similar to a RANS model. The equations solved in the SRH model are ascertained using a spatial-temporal filtering, i.e. each variable ϕ is decomposed into a filtered $\overline{\overline{\phi}}$ and a subfiltered value ϕ′ as per:

$$\phi = \overline{\overline{\phi}} + \phi' \tag{2}$$

where φ is representative of quantities such as velocity components, pressure, and energy. Duffal et al. [30] details further information relating to the SRH model utilised in the CFD investigations.

The decomposed solution variables from the SRH model are input into the Navier-Stokes equations to yield filtered transport equations of mass, momentum, and energy. The time-dependent Navier-Stokes (governing) equations of the flow-field are defined as:

$$\nabla \cdot u = 0 \tag{3}$$

$$\rho \frac{\partial u}{\partial t} + \rho(u \cdot \nabla)u + \nabla p = \mu \nabla^2 u \tag{4}$$

where u is the velocity vector, and p is the pressure. The investigations were completed using a segregated pressure-based flow solver on a finite volume implementation in Star-CCM+ with a timestep of 0.001s. A SIMPLE (Semi-Implicit method for pressure-linked equations) pressure-velocity coupling algorithm was used, in addition to optimised 2nd-order temporal discretisation. This reduces the leading-order truncation error by a factor of 2, compared to base-level 2nd-order temporal discretisation [31].

2.4.2. Non-Newtonian model and haemodynamic metrics

Often it is reasonable to use a Newtonian fluid model to approximate the rheology of blood in computational haemodynamics. This is applicable when the areas of interest are exposed to high shear throughout the domain during the cardiac cycle, which suppresses the rouleaux formation. A Newtonian rheology assumption omits the 'shear-thinning' property of blood, which manifests at shear rates below $50-100s^{-1}$. Due the size of the AVF vessels, the produced shear rates would stretch the Newtonian rheology assumption. Therefore, a generalised Carreau-Yasuda non-Newtonian model [21] was implemented with values from literature (Supplementary Material). The time-averaged WSS (TAWSS) and oscillatory shear index (OSI) [22,23,26] are key haemodynamic metrics, described as:

$$TAWSS = \frac{1}{T}\int_0^T |\tau_w| dt \tag{5}$$

$$OSI = \frac{1}{2}\left(1 - \frac{\left|\int_0^T \tau_w \, dt\right|}{\int_0^T |\tau_w| \, dt}\right) \tag{6}$$

where t is the time, T is the cardiac cycle time, and τ_w is the wall shear stress. TAWSS evaluates shear stress exerted on the vessel walls during the cardiac cycle, whereas OSI assesses the directional change of WSS during the cardiac cycle. We present TAWSS as a normalised quantity, where the TAWSS values are normalised with respect to the predicted TAWSS generated at the ascending aorta inlet in the pre-AVF case. The value of TAWSS predicted at the inlet was 27.5Pa via the computation of:

$$\tau_w = \mu \frac{\mathrm{du}}{\mathrm{dy}} = \left[\frac{-4\mu u_{max}}{D_{inlet}}\right] \tag{7}$$

where u_{max} is the peak fluid velocity maxima, and D_{inlet} is the inlet vessel diameter.

Additionally, the Reynolds number (Re), a dimensionless ratio of fluid momentum to viscous shear force, was computed for flow analysis at various locations within the fistula. Mean and maximum Re values were calculated, respectively, according to:

$$Re_{mean} = \frac{u_{mean} \cdot D}{\mu} \tag{8}$$

$$Re_{\max} = \frac{u_{\max} \cdot D}{\mu} \tag{9}$$

where u_{mean} is the mean flow velocity, u_{max} is the local maximum flow velocity, and D is the local cross-sectional diameter normal to the centreline of the domain.

2.4.3. Boundary conditions

Triphasic velocity inlet waveforms based on the cardiac output measured at the pre-surgical ($CO_{pre\text{-}AVF}$ = 6.49 L/min) and post-operative ($CO_{post\text{-}AVF}$ = 8.03 L/min) visits were assigned at the aortic root in each respective simulation (Fig. 1). A no-slip rigid wall condition was assumed in each of the simulations. The majority of arterial outlet branches in both the pre- and post-AVF simulations were treated as pressure outlets, with each of them being coupled to lumped-parameter

three-element Windkessel (WK) models [32] (Supplementary Material). The exceptions were the venous and arterial vessels distal to the created AVF in the post-AVF case (the cephalic vein and radial artery outlets), which were assigned flow waveforms based on post-operative FeMRA scanning (Supplementary Material). With regard to the WK models, the capacitance (C) and resistance (R) parameters account for the compliance and peripheral resistance of the terminal branch, respectively, while the characteristic impedance element (Z) represents the resistance of the terminal vessel. The expression relating the flow rate (Q) and pressure (p) in the 3-element WK model with respect to time (t) [33] is expressed by:

$$\frac{\partial p}{\partial t}+\frac{p}{RC}=\frac{Q}{C}\left(1+\frac{Z}{R}\right)+Z\left(\frac{\partial Q}{\partial t}\right) \tag{10}$$

The discretisation of this model in the time-domain for purposes of a time-discretised CFD study, yields:

$$p^{n+1}=\frac{\frac{\tau}{\Delta t}p^{n}+Q^{n+1}\left(R+Z\left(1+\frac{\tau}{\Delta t}\right)\right)-Z\frac{\tau}{\Delta t}Q^{n}}{1+\frac{\tau}{\Delta t}} \tag{11}$$

where τ=RC, p and p^{n+1} are the pressure at the current and next timestep, Q and Q^{n+1} are the volumetric flow rates at the current and next timestep, and Δt is the timestep.

The use of 3-element WK models produced physiologically relevant pressure values (120/80 mmHg) in both simulations. This approach compared favourably with respect to the 'splitting method' [34] (22/-8mmHg), which involved computing branch diameters immediately following a bifurcation (see Supplementary Material). The

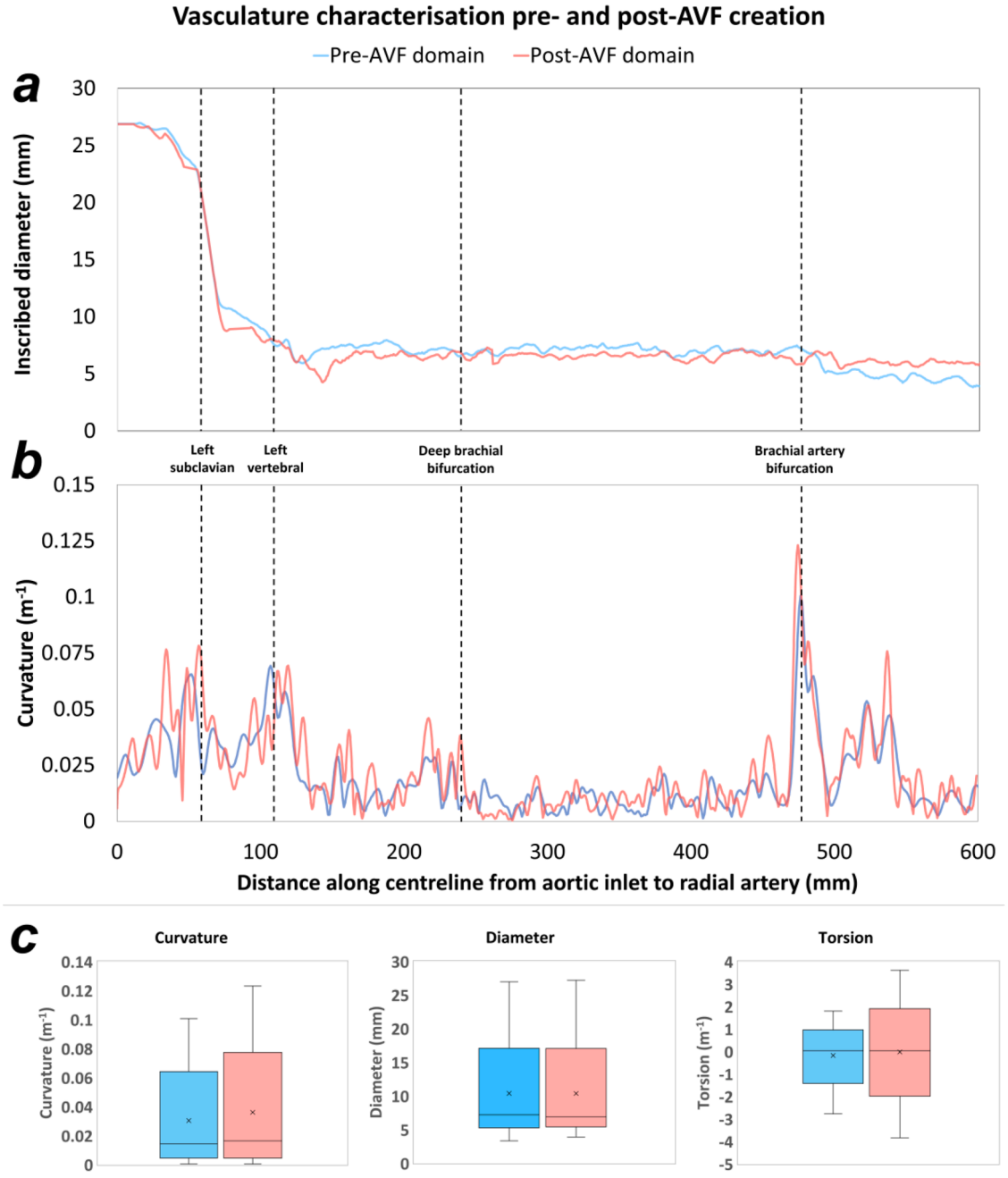

Figure 4. Pre- (blue) and post-AVF (red) centreline characteristics, where (a) and (b) show inscribed vessel diameter and centreline curvature from the aortic inlet to the radial artery, and (c) shows the curvature, diameter, and torsion box plots of the centerline from the ascending aorta (AscA) to descending aorta (DSA) and left radial artery (LRA) outlets. (For interpretation of the references to color in this figure legend, the reader is referred to the web version of this article.)

capacitance and resistive values of each 3-element WK model are dependent on the artery's characteristics in addition to the distal vasculature. An estimate for the characteristic impedance (Z) and capacitance of each terminal artery (C_0) is given by:

$$Z = \frac{\rho \cdot c_d}{A_d} \tag{12}$$

$$C_0 = \frac{A_d L}{\rho (c_d)^2} \tag{13}$$

where L, c_d, and A_d are the vessel length, pulse wave velocity (PWV) and vessel area at diastolic pressure, respectively. Characteristic R and C values for each 3-element WK model can subsequently be calculated with the methodology detailed in Alastruey [35] (Supplementary Material), using the following equations:

$$R = \left(\frac{1}{1 - \frac{\lambda}{2\phi^4}} - 1 \right) Z = \left(\frac{\lambda}{2\phi^4 - \lambda} \right) Z \tag{14}$$

$$C = \left(\frac{1}{1 - 2\lambda\phi^3} - 1 \right) C_0 = \left(\frac{2\lambda\phi^3}{1 - 2\lambda\phi^3} \right) C_0 \tag{15}$$

where λ=0.7 and $\phi = \sqrt{0.6}$ are estimated using the techniques described in [35,36]. Further information is provided in Supplementary Material.

3. Results

The results are presented in three parts: a geometrical characterisation of the pre- and post-fistula geometries is described first (Figs. 4, 5), an analysis of the global haemodynamics from the aorta to the radial artery (pre-AVF) and radiocephalic AVF (post-AVF) is provided second (Figs. 6–9), followed by the localised flow development in the remodelled patient-specific arteriovenous fistula, 6-weeks post-surgery (Fig. 10) at three intervals of the cardiac cycle: peak systole (T1), mid-deceleration (T2), and peak diastole (T3).

3.1. Pre- and post-fistula geometry characterisation

In order to characterise the geometries, the centrelines of each computational domain were computed utilising the VMTK libraries (http://www.vmtk.org). The changes in inscribed diameter and curvature along the length of the centreline from the ascending aorta (inlet) to the left radial artery is presented for both cases in Fig. 4a and 4b, respectively, to ensure valid comparisons can be made between the reconstructed geometries due to consistent segmentation. With the same imaging protocol (Supplementary Material) and segmentation method being used, differences in the proximal vasculature characteristics are considered to be due to minor differences in the original image acquisition and segmentation. However, the haemodynamic origins and remodeling are thought to be the causations of increased radial artery diameters in the post-AVF. Box plots of curvature, diameter, and torsion for these centrelines also confirm that the geometries do not differ greatly (Fig. 4c).

The localised dimensions of the patient-specific AVF studied here are presented in Fig. 5, demonstrating successful AVF maturation with respect to the 'rule of six', i.e. the venous diameter exceeding 6mm at 6-weeks post-AVF creation. This is in accordance with the National Kidney Foundation's Kidney Disease Outcomes Quality Initiative (KDOQI) vascular access guidelines [6]. The anatomical characteristics of the AVF is of crucial importance to AVF success and usability.

3.2. Aorta-to-radial artery haemodynamics

Fig. 6a demonstrates the changes in the haemodynamic environment proximal to the fistula for the pre- and post-AVF vasculatures through velocity streamlines at peak systole. Fig. 6b displays the flow rate waveforms at three locations along the left arm (the left subclavian, brachial and radial arteries) before and after the creation of the AVF. The velocity streamline and flow rate values in the post-AVF case reflect the decrease in peripheral resistance and increased flow rate, particularly in the radial artery, arising from the anastomosis creation. Between the pre-operative and post-surgical simulation, the maximum localised Reynolds number (Re_{max}) in the left subclavian, brachial, and radial arteries was significantly influenced, increasing by over a factor of 2 in each case (Fig. 6). The value of Re_{max} (calculated using the flowrates in Fig. 6b) in the left subclavian artery (at location α, α′) increased by a factor of 2.13 (706 to 1504), the left brachial Re_{max} value (at location β, β′) increased by a factor of 2.47 (537 to 1328), and the value of left radial Re_{max} (at location γ, γ′) increased by a factor of 2.37 (890 to 2106).

The overall trend in the proximal haemodynamics is demonstrated through analysis of the Re_{max} numbers at the outlets of the simulated vasculature (Fig. 7). Despite the increased cardiac output in the post-AVF case, the vessels not associated with the left arm (i.e. the vessels

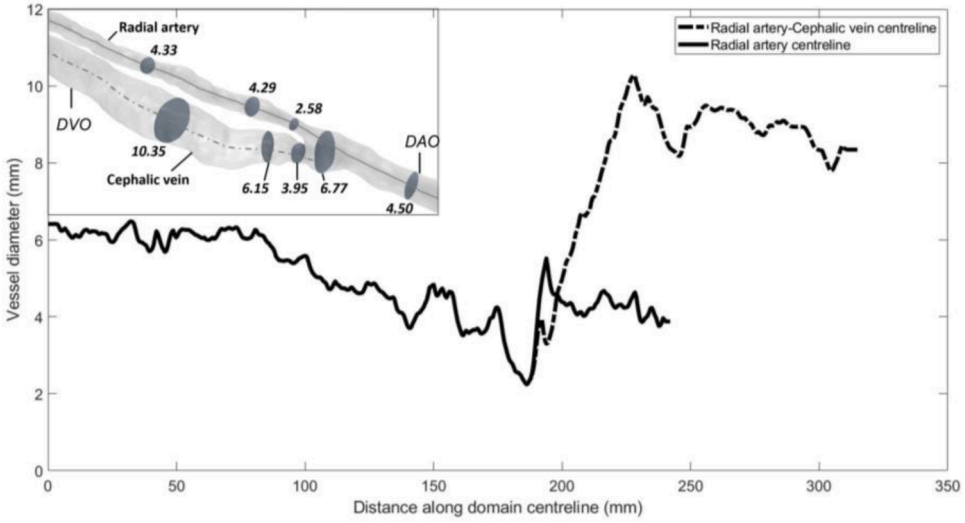

Figure 5. Change in inscribed vessel diameter (normal to vessel centrelines) near the AVF with respect to the distance along the domain centreline from the feeding (radial) artery (starting from 195mm proximal to the anastomosis) to the draining vessels.

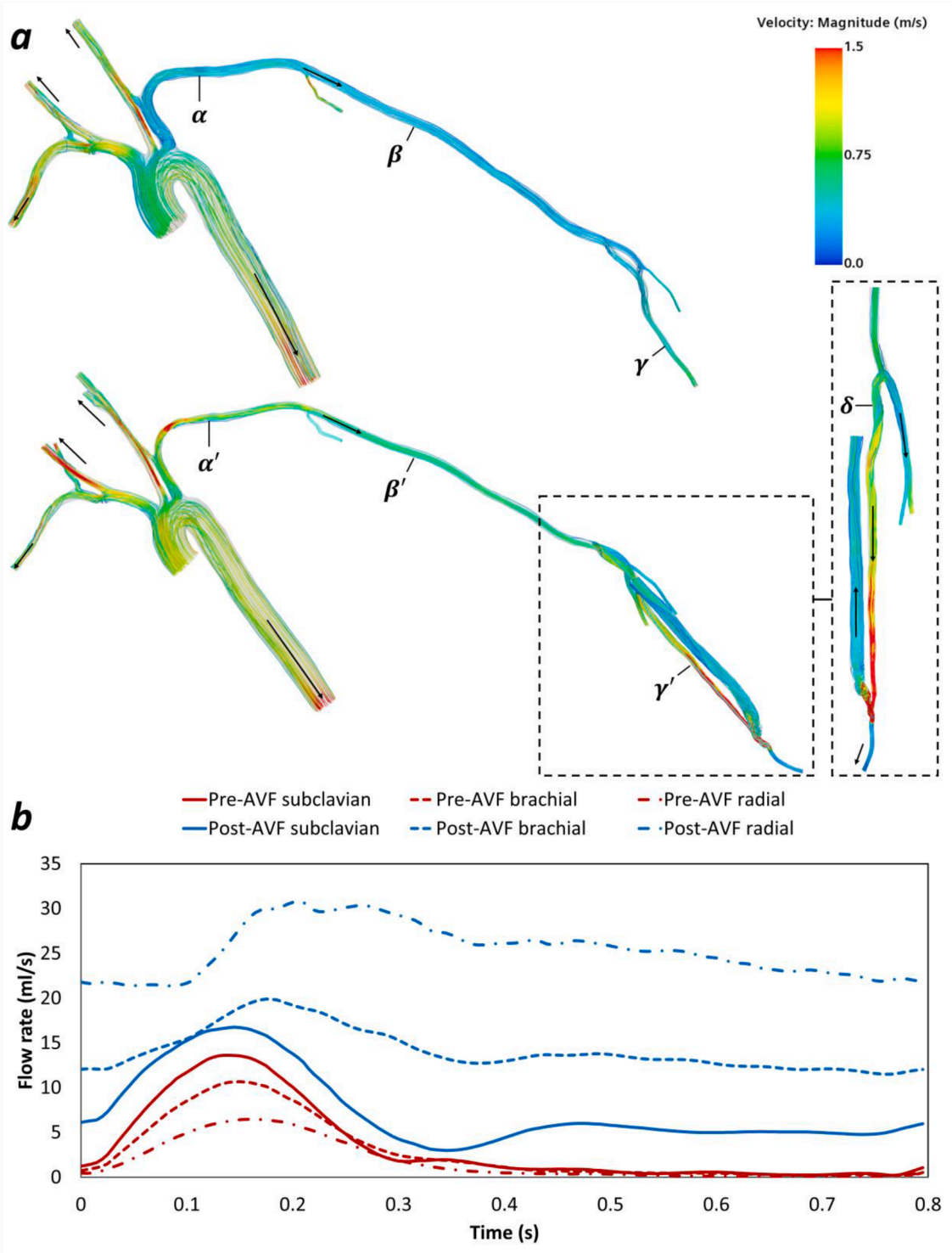

Figure 6. (a) Velocity streamlines pre- and post-AVF at peak systole (where arrows represent flow direction), (b) flow rate waveforms in the vasculature at (α, α') the left subclavian, (β, β') brachial, and (γ, γ') radial arteries pre- and post-AVF creation.

not on the centreline trajectory towards the AVF) have less flow when compared to the pre-AVF case. The mean Re_{mean} number in the left common carotid, right common carotid, left vertebral, right vertebral, and right subclavian arteries is lower in the post-AVF case than the pre-AVF case. The opposite is true for the left deep brachial, left interosseous, left ulnar, and left radial arteries, where the Re_{mean} number is significantly increased.

The results from this simulation have been validated through analysis and comparison of the CFD results and phase-contrast FeMRA-obtained data in the left radial artery following anastomosis creation (Fig. 8). The mean percentage difference between the CFD and phase-contrast FeMRA in the radial (feeding) artery was calculated to be 2.52%.

The increased velocity in the left arm vasculature induced by the anastomosis creation resulted in considerably increased TAWSS values throughout the left arm, that is the left subclavian, deep brachial, brachial, radial, ulnar, and interosseous arteries (Fig. 9a). The locations of the vasculature with normalised TAWSS (NormTAWSS) exceeding 1.0

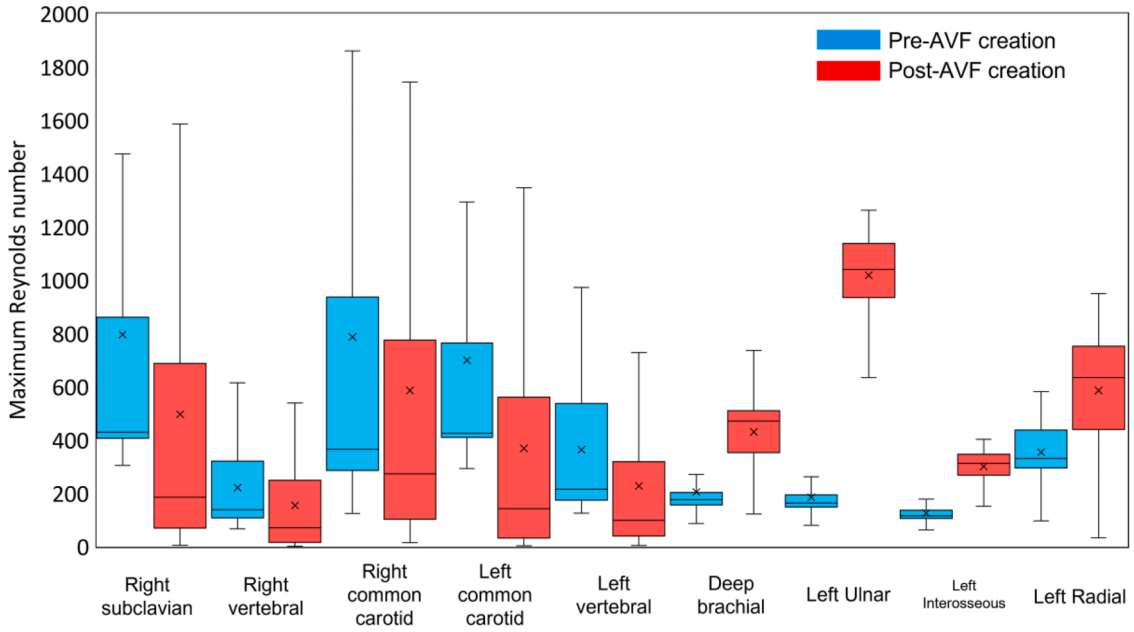

Figure 7. Box and whisker plots of the Re_{max} values at the outlets of the simulated vasculature induced over the analysed (5th) cardiac cycle in the common simulated vasculature between the pre- and post-AVF cases. The Re_{mean} values are denoted with a straight line within each box.

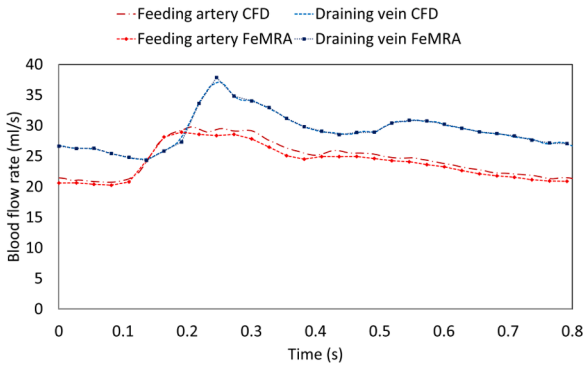

Figure 8. Comparison between the patient-specific phase-contrast FeMRA-obtained volumetric flow rate at the radial (feeding) artery (red dot dash line) and the flow waveform generated computationally in the radial artery (red dash line). The radial artery was assessed at location δ as shown at the inset of Fig. 6a. The cephalic vein (blue dot dash line) prescribed waveform at the venous outlet is also presented. (For interpretation of the references to color in this figure legend, the reader is referred to the web version of this article.)

include the left subclavian, radial, and ulnar arteries. The most prominent of these regions is the radial artery, where NormTAWSS exceeded the value of 10.0 at the anastomosis location. This is in part due to luminal narrowing. NormTAWSS values exceeded 1.0 also immediately following the AVF anastomosis in both the 'draining artery' and 'draining vein'. Regarding the other regions of the proximal vasculature, the NormTAWSS remained largely unaffected, which is supported by the small change in the localised Re_{max} values (Fig. 7). This is due to velocity values impacting WSS magnitudes (as velocity correlates to the shear stress between fluid and vessel wall), in accordance with Eq. 7.

Furthermore, there are significant changes in the OSI contour plot distribution due to the AVF creation (Fig. 9b). Pre-AVF formation, OSI levels of ~0.3 were measured in the left subclavian and brachial arteries, with OSI levels of ~0.15 in the left radial, ulnar, and interosseous arteries. Following the anastomosis creation, the OSI levels measured in the left arm vasculature are negligible, the only exceptions being the peri-anastomotic region in the draining vessels of the AVF, where OSI is prominent. These results infer that there is minimal directional change in WSS during the cardiac cycle in the left arm vessel proximal to the AVF. However, there are changes in the OSI profiles of the thoracic aorta, with increased OSI levels in various parts of the descending aorta following AVF creation. Lastly, the OSI levels remain similar in magnitude and profile in the common carotid, vertebral, and right subclavian arteries.

3.3. Localised haemodynamics at the AVF anastomosis

The non-physiological flow induced by the anastomosis exceeded 4m/s in the left radial artery throughout the cardiac cycle and at the presented time intervals (Fig. 10a-c). In the cephalic vein, the velocity streamlines exhibited transitional flow with values below 2m/s, however this equates to a mean flow rate in excess of 1750ml/min, and a maximum flow rate of 2275ml/min (local Re_{max}=3386). Downstream of the fistula in the draining vein, helical flow patterns were characteristically evident throughout the cardiac cycle, which persisted along the entire length of the cephalic vein. Retrograde flow was also observed in the 'draining' (radial) artery at mid-deceleration and peak diastole (Fig. 10b-c). Fig. 10d and e present an enlarged view of the normalised TAWSS and OSI distributions shown in Fig. 9a and b, respectively, around the localised AVF geometry. It is noted that NormTAWSS is shown in Fig. 10d at a different range than in Fig. 9a to highlight localised differences. Significantly high NormTAWSS values (>10.0) were observed in the feeding (radial) artery of the AVF, at the apex of the anastomosis, and on the venous side of the anastomosis. This is due to the luminal narrowing of the feeding artery juxta-anastomosis (Fig. 5) and the rapid change in flow direction through the AVF. NormTAWSS progressively decreased along the venous and arterial outlet branches to much lower values at short distances from the fistula. The scale of the normalised TAWSS plot was revised to demonstrate the significant normalised WSS values present at the anastomosis location, which greatly exceed the values in the feeding artery. Notably high OSI magnitudes (in the value range of 0.35-0.45) were observed in the distal artery branch of the AVF, in contrast to the negligible OSI values found upstream of the anastomosis (as shown in Fig. 9b). High OSI magnitudes were also observed in the venous segment, notably at the apex of the anastomosis and two distal regions where the venous segment has successfully expanded to diameter greater than 6mm.

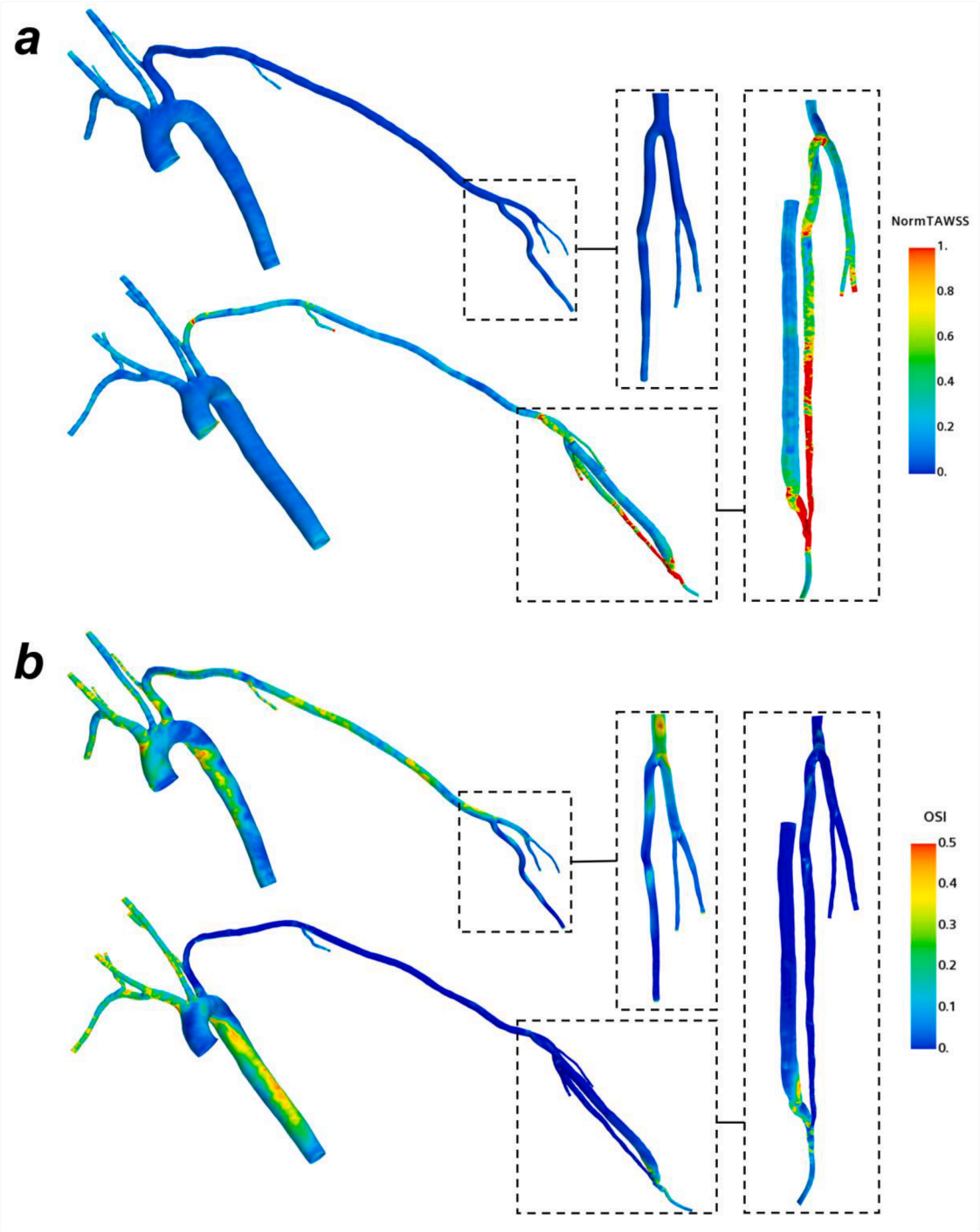

Figure 9. (a) Normalised TAWSS and (b) OSI contour plots prior-to and after fistula creation.

4. Discussion

The presented framework of generating a patient-specific geometry from high-resolution FeMRA scans of a young patient with CKD has demonstrated its potential for subsequent patient-specific AVF CFD investigations. This has been an area of difficultly in prior AVF CFD research, where challenges exist in contrast enhancement. Utilising the presented framework can support greater numbers of patient-specific AVF CFD investigations, which can contribute to a previously proposed patient-care centred approach [6]. The dimensions of the generated domains in this research were validated with respect to the original DICOM stacks. The methods used in the CFD simulations, such as the implementation of 3-element Windkessel models, are standard in computational haemodynamics. The assigning of flow waveforms (from phase-contrast data) to the 'draining vessels' of the AVF in the post-AVF case was necessary to produce the correct haemodynamic environment and to account for the retrograde and antegrade flow that is present at the 'draining artery' outlet.

The mean percentage difference between the CFD and phase-contrast FeMRA velocity magnitude data (using a surface average of the vessel cross-section) in the radial artery was calculated to be 2.52%, providing a good validation of the CFD results. Replicating the flow conditions in the reconstructed geometry permitted analyses of haemodynamic metrics juxta-anastomosis in addition to analysing the influence of increased

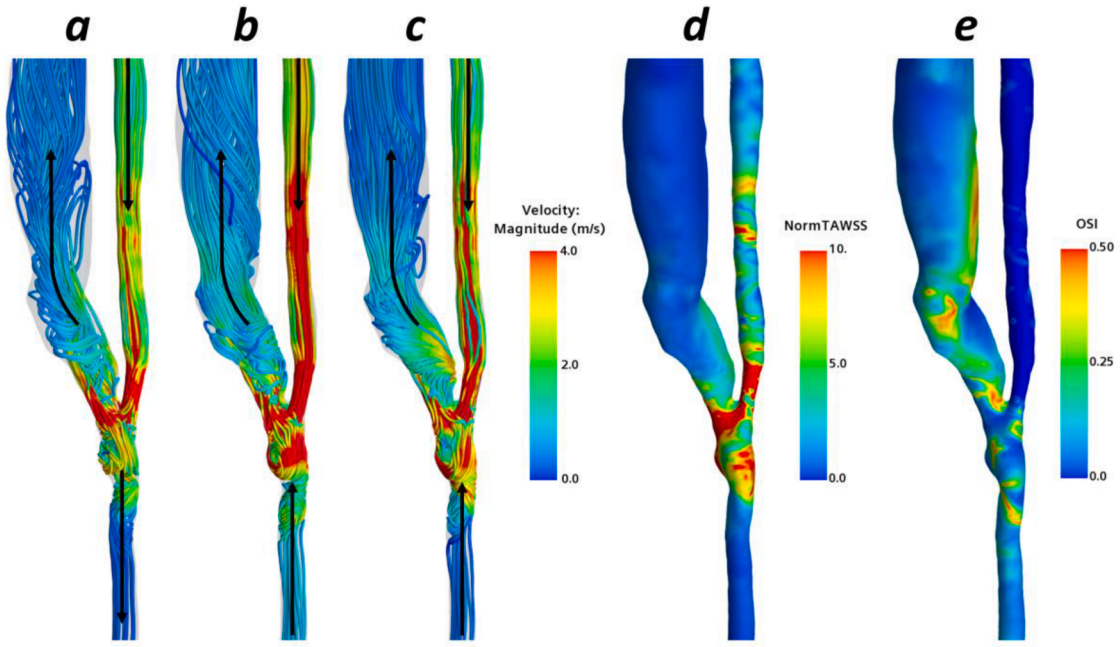

Figure 10. (a-c) Velocity streamlines and flow directions (arrows) in the radiocephalic fistula anastomosis at (a) T1 (peak systole), (b) T2 (mid-deceleration), and (c) T3 (peak diastole). (d) Normalised TAWSS, (e) OSI.

cardiac output on the vasculature proximal to the AVF. The key finding from this study was the marked increase in blood flow velocity and TAWSS demonstrated throughout the left subclavian, brachial, and radial arteries unilaterally to the AVF. This is a marker of adaptive arterial remodelling to accommodate the increased flow rates resulting from the surgical anastomosis. In addition, the diameter of the specific reconstructed AVF was suggestive of successful fistula maturation [6]. The localised haemodynamic factors relating to NH and outward remodelling were analysed confirming sufficient AVF flow rates (>600mL/min) and the generation of transitional flow with substantial helical flow patterns in the cephalic vein distal to the anastomosis throughout the cardiac cycle. This arises due to the significant change of direction of the flow entering the vein, which generates complex vortices and secondary flows when flow is exerted on the opposite vessel wall. Our simulation indicated cyclic disturbed flow (OSI 0.42) in the radial artery distal to the anastomosis, and in the vein immediately following the venous swing segment of the AVF. This region of the vein, which experiences low and oscillatory shear stress, corresponds to where luminal reduction may occur due to NH. This hypothesis is reinforced in the findings of Ene-Iordache et al. [17] and Niemann et al. [37] in similar AVF configurations. Due to the structure of AVFs, a degree of NH is inevitable and is even observed in functional fistulae. However, further elucidation of the flow mechanisms in AVFs may minimise NH.

4.1. Limitations

A limitation in this work was the assumption of rigid walls, however, this is a common approach in computational haemodynamics. The influence of arterial wall deformation on the haemodynamic environment of large vessels is considered relatively small, however, for the juxta-anastomosis environment, wall motion effects may be more pronounced. Fluid-structure interaction (FSI) methodologies can account for this behaviour but FSI modelling is challenging and requires considerable computational expense. Another key reason for omitting FSI influence from the CFD investigation was the selection of the boundary conditions. Using a prescribed outflow waveform ascertained from phase-contrast data for the AVF draining vessels meant that the flow conditions within the AVF were replicated as closely as possible. The utilisation of a polynomial triphasic aortic inlet waveform calculated using cardiac output data at each visit is also a minor limitation of the CFD study, as the results at peak systole may be slightly different in reality. Another assumption was that only a single patient was examined in the study. Finally, the selection of Windkessel parameter values can also be considered a limitation due to the resistances and capacitances being estimated as per the 'Boundary conditions' subsection. The same Windkessel values were assumed for the terminal arteries in the pre- and post-AVF simulation (apart from the AVF vessels), which is also a potential limitation.

4.2. Comparisons to prior work

Prior work has been completed on coupling MRI and CFD [38], and Bozzetto et al. [39] demonstrated good quality images in a short scan duration when coupling contrast-free MRI and CFD. To our knowledge, the present study is the first to couple FeMRA with CFD, particularly to describe AVF dynamics. The majority of CFD studies on AVF haemodynamics focus on the local environment at the site of the anastomosis [40, 41]. For example, Cunnane et al. [42] studied varying anastomosis angles and their influence on the WSS distribution, while Niemann et al. [37] examined WSS in six different fistula morphologies. In addition to analysing the local haemodynamics at the anastomosis, our study expands current knowledge by assessing the blood flow dynamics proximal to the fistula, which has not been studied before. Kroon et al. [43] reviewed the potential use of a patient-specific vascular low-order network model for predicting haemodynamic changes in the network six weeks after AVF creation. However, 3D numerical investigations, such as those presented in this paper, permits a more comprehensive analysis of the haemodynamics than low-order models, despite the inevitably increased computational expense, which is nonetheless lower than FSI simulations.

4.3. Clinical relevance

The time required for completing this workflow from initial segmentation to CFD post-processing was approximately 6 h (for an experienced user of the software). The benefit of using CFD in addition to FeMRA is the profiling of haemodynamic metrics that are difficult to

measure *in-vivo*. This is highly relevant for the identification of probable sites of atherosclerotic lesion development proximal to the AVF, and the factors relating to perianastomotic intimal hyperplasia and inadequate outward remodelling at the outflow vein. The current consensus, particularly for adults and older ages, is that atherosclerosis usually occurs in arterial regions of low and/or oscillatory WSS [44]. Furthermore, atherosclerotic development typically occurs at wall curvature locations and bifurcations, such as the brachiocephalic trunk, a known location for atherosclerotic lesion development that is also reflected in our results. The atherosclerotic regions identifiable in the TAWSS and OSI contour plots are limited, with low OSI regions in the left arm having high TAWSS values. Conversely, the comparably low TAWSS regions in the aorta, carotid, and vertebral arteries have high OSI values. A small region of potential atherosclerotic development would be a region of left subclavian branch immediately following its bifurcation from the aortic arch, which is due to its comparably low TAWSS values.

In addition to this, the increase in flow velocity and TAWSS at various locations post-AVF indicates likely arterial remodelling [45] proximal to the location of the AVF. These markers were undermined in prior AVF studies, which focused predominately on localised AVF haemodynamics, or in some cases, the AVF's influence on cardiac volume. The impact of arterial remodelling on the arm vessels proximal to the AVF may be detrimental to the patient through increased predisposition to other complications, such as cardiovascular disease and arterial steal syndrome. Further elucidation of important potential complications can be made using more thorough CFD analysis with boundary conditions set by post-AVF patient flow data at several locations in the vasculature. The favourable hypothesis of high TAWSS causing outward remodelling for increased flow rates is also partially considered as a potential factor towards future endothelial damage. Despite the exact pathophysiology not being known, endothelial WSS triggers biomedical and biological events. Evidence suggests perturbed stress and strains disturb the biochemical homeostasis [17] and cause adverse vascular remodelling and potential dysfunction. In addition to endothelial dysfunction, a harbinger of atherosclerosis, low WSS levels have been associated with an increase in neointima formation, and a proclivity toward vein vasoconstriction [46]. However, NH lesions associated with AVFs differ from atherosclerotic lesions. NH occurs due to the proliferation of vascular smooth muscle cells, in addition to neovessels and inflammatory cells. Furthermore, optimal venous endothelial function has been associated with moderate-to-high WSS levels due to the quiescence and alignment of endothelial cells under laminar flow conditions.

The WSS levels modelled by CFD (Fig. 10d) indicate the successful maturation of the AVF. This is identified as the TAWSS values induced in the venous segment (cephalic vein) of the AVF (Figs. 9a, 10d) have reduced to baseline levels (<2Pa) following the high WSS levels induced during the creation of the anastomosis. The WSS values correspond to magnitudes reported in prior computational AVF studies [12,45,47]. This reflects the desired situation at six weeks post-AVF creation with respect to the 'rule-of-six' [6], where the flow rate exceeds 600mL/min whilst the venous diameter has exceeded 6mm to accommodate the increased flow rate. These conditions are achieved due to the outward remodelling of the cephalic vein, which occurs in conjunction with the maturation of the AVF. Despite the successful maturation and outward remodelling of the AVF, high TAWSS and low OSI values juxta-anastomosis are inevitable due to the rapid redirection of flow. Therefore, in a successful AVF, these vessel regions remain at risk to atherosclerotic and neointimal complications.

4.4. Conclusions and further work

This is the first study to demonstrate detailed dynamics of pulsatile blood flow from the aortic root to the distal arm arteries prior to and following AVF creation. Moreover, the use of CFD with FeMRA in this study demonstrates the potential for more thorough explanation of the complex haemodynamics associated with patient-specific AVF creation. Haemodynamic changes in the proximal vessels are of clinical importance for AVF maturation, NH and cardiovascular impact, while a central vein (or cephalic arch) stenosis is a common cause of AVF dysfunction and failure. For that purpose, a new methodological framework was presented involving the geometry reconstruction from multiple stacks of FeMRA-obtained medical images of a young patient. This is an important step towards understanding the blood flow development proximal to the arm region where an AVF is created in ESKD patients. The last part of the study involved a detailed haemodynamic analysis of the flow around a patient-specific AVF. This is advantageous in the pre-surgical planning and post-operative evaluation of AVFs, as the arterial blood flow and cross-sectional diameter before AVF formation is known to correlate with its maturation [48]. Additionally, the post-AVF venous blood flow rates relate to AVF maturation, hence analysis of the juxta-anastomosis haemodynamics becomes crucial in relation to success and failure rates. WSS is of high importance in this case, as outward remodelling occurs to reduce the WSS in the AVF over time [49]. The remodelling is associated with the increase in vessel diameter required for the increased flow rates.

Further work will seek to investigate the differing haemodynamic environments in a cohort of patients with varying AVF anastomoses configurations and outcomes (success versus failure). This will include brachiocephalic fistulae in addition to radiocephalic fistulae. Additionally, the arterial wall motion will be accounted for in future numerical simulations of the local AVF haemodynamics by incorporating an FSI element into the investigation.

Funding

This work is supported in part from the University of Strathclyde International Strategic Partner Research Studentships, the UK Research and Innovation (UKRI) Engineering and Physical Sciences Research Council (EPSRC) Award Ref. EP/W004860/1 via the Transformative Healthcare Technologies scheme, and the EU H2020 research and innovation programme under the Marie Sklodowska-Curie grant agreement No 749185.

Ethics

Patient-specific data presented here are derived from a previously published prospective comparative study [50]. The study protocol (https://doi.org/10.36399/gla.pubs.215112) was approved by the institutional review board (Research Ethics Committee Reference: 16/NS/0099) and registered with ClinicalTrials.gov (NCT02997046). Written informed consent was obtained from all participants.

Declaration of Competing Interest

The authors declare no conflict of interest regarding the publication of this article.

Acknowledgment

The authors greatly acknowledge the support from the University of Strathclyde and the Queen Elizabeth University Hospital (Glasgow, UK).

Supplementary materials

Supplementary material associated with this article can be found, in the online version, at doi:10.1016/j.medengphy.2022.103814.

References

[1] Cockwell P, Fisher L. The global burden of chronic kidney disease. Lancet 2020;395 (10225):662–4.
[2] Okada S, Shenoy S. Arteriovenous access for hemodialysis: Preoperative assessment and planning. J Vasc Access 2014;15(S7):S1–5.

[3] Brescia MJ, et al. Chronic hemodialysis using venipuncture and a surgically created arteriovenous fistula. N Engl J Med 1966;275(20):1089–92.
[4] Guyton AC, Sagawa K. Compensations of cardiac output and other circulatory functions in areflex dogs with large av fistulas. Am J Physiol Legacy Content 1961; 200:1157–63.
[5] Robbin ML, et al. Arteriovenous fistula development in the first 6 weeks after creation. Radiology 2016;279(2):620–9.
[6] Lok CE, et al. Kdoqi clinical practice guideline for vascular access: 2019 update. Am J Kidney Dis 2020;75(4):S1–164. S2.
[7] Feldman HI, et al. Hemodialysis vascular access morbidity. Clin J Am Soc Nephrol 1996;7(4):523–35.
[8] Polkinghorne KR, et al. Vascular access and all-cause mortality: a propensity score analysis. Clin J Am Soc Nephrol 2004;15(2):477–86.
[9] Wong C, et al. Vascular remodeling and intimal hyperplasia in a novel murine model of arteriovenous fistula failure. J Vasc Surg 2013;59(1):192–201.
[10] Remuzzi A, et al. Is shear stress the key factor for AVF maturation? J Vasc Access 2017;18:10–4.
[11] Hull J, et al. Computational fluid dynamic evaluation of the side-to-side anastomosis for arteriovenous fistula. J Vasc Surg 2013;58(02).
[12] Sigovan M, et al. Vascular remodeling in autogenous arterio-venous fistulas by MRI and CFD. Ann Biomed Eng 2013;41(4):657–68.
[13] Stern A, Klemmer P. High-output heart failure secondary to arteriovenous fistula. Hemodial Int 2011;15(1):104–7.
[14] Kumar A, et al. Radiomedian cubital /radiocephalic arteriovenous fistula at elbow to prevent vascular steal syndrome associated with brachiocephalic fistula: review of 320 cases. Indian J Urol 2007;23(3):261–4.
[15] Roy-Chaudhury P, et al. Predicting dialysis vascular access blood flow and diameter: too much, too little, or just right. Kidney Int 2013;84(6):1076–8.
[16] Bozzetto M, et al. Transitional flow in the venous side of patient-specific arteriovenous fistulae for hemodialysis. Ann Biomed Eng 2016;44(8):2388–401.
[17] Ene-Iordache B, Remuzzi A. Disturbed flow in radial-cephalic arteriovenous fistulae for haemodialysis: low and oscillating shear stress locates the sites of stenosis. Nephrol Dial Transp 2012;27(1):358–68.
[18] Ene-Iordache B, et al. Computational fluid dynamics of a vascular access case for hemodialysis. J Biomech Eng 2001;123(3):284–92.
[19] Zhu Y, et al. Clinical validation and assessment of aortic hemodynamics using computational fluid dynamics simulations from computed tomography angiography. Biomed Eng Online 2018;17(53).
[20] Johnston L, et al. Hemodynamics in the aorta and pulmonary arteries of congenital heart disease patients: a mini review. J Cardiol Cardiovasc Sci 2021;5(2):1–5.
[21] Boumpouli M, et al. Blood flow simulations in the pulmonary bifurcation in relation to adult patients with repaired tetralogy of fallot. Med Eng Phys 2020;85: 123–38.
[22] Kazakidi A, et al. Effect of reverse flow on the pattern of wall shear stress near arterial branches. J R Soc Interface 2011;8:1594–603.
[23] Kazakidi A, et al. Effect of Reynolds number and flow division on patterns of haemodynamic wall shear stress near branch points in the descending thoracic aorta. J R Soc Interface 2009;6:539–48.
[24] Boumpouli M, et al. Characterization of flow dynamics in the pulmonary bifurcation of patients with repaired Tetralogy of Fallot: a computational approach. Front Cardiovasc Med 2021;8:703717. https://doi.org/10.3389/fcvm.2021.703717.
[25] Johnston L, et al. Hemodynamic abnormalities in the aorta of turner syndrome girls. Front Cardiovasc Med 2021;8:670841. https://doi.org/10.3389/fcvm.2021.670841.
[26] Van Doormaal MA, et al. Haemodynamics in the mouse aortic arch computed from mRI-derived velocities at the aortic root. J R Soc Interface 2012;9:2834–44.
[27] Stoumpos S, et al. Ferumoxytol-enhanced magnetic resonance angiography for the assessment of potential kidney transplant recipients. Eur Radiol 2018;28(1): 115–23.
[28] Yushkevich P, et al. User-guided 3D active contour segmentation of anatomical structures: significantly improved efficiency and reliability. Neuroimage 2006;31 (3):1116–28. Jul 1.
[29] Broadhead BL, et al. Sensitivity and uncertainty-based criticality safety validation techniques. Nucl Sci Eng 2004;146(3):340–66.
[30] Duffal, V., et al. Development and validation of a hybrid RANS-LES approach based on temporal filtering. Proc. of the 8th Joint Fluids Engineering Conference, San Francisco, USA. 2019.
[31] Vatsa V, et al. Re-evaluation of an Optimized Second Order Backward Difference (BDF2OPT) Scheme for Unsteady Flow Applications. 48th AIAA Aerospace Sciences Meeting Including the New Horizons Forum and Aerospace Exposition 2010. https://doi.org/10.2514/6.2010-122.
[32] Westerhof N, et al. An aid for clinical research and graduate education. Snapshots of Hemodynamics. Springer International Publishing, AG; 2018.
[33] Pirola S, et al. On the choice of outlet boundary conditions for patient-specific analysis of aortic flow using computational fluid dynamics. J Biomech 2017;60: 15–21.
[34] Chnafa C, et al. Better than nothing: A rational approach for minimizing the impact of outflow strategy on cerebrovascular simulations. Am J Neuroradiol 2018;39(2): 337–43.
[35] Alastruey Arimon, J. Numerical modelling of pulse wave propagation in the cardiovascular system: development, validation and clinical applications. PhD thesis, Imperial College, London, UK, 2006.
[36] Papageorgiou GL, Jones NB. Wave reflection and hydraulic impedance in the healthy arterial system: a controversial subject. Med Biol Eng Comput 1988;26(3): 237–42.
[37] Niemann A, et al. Computational fluid dynamics simulation of av fistulas: From mri and ultrasound scans to numeric evaluation of hemodynamics. J Vasc Access. 1 2011;3(1):36–44.
[38] Ha H, et al. Fluid-dynamic optimal design of helical vascular graft for stenotic disturbed flow. PLoS One 2014;9(10):e111047.
[39] Bozzetto M, et al. Toward longitudinal studies of hemodynamically induced vessel wall remodeling. Int J Artif Organs 2018;41(11):714–22.
[40] Grechy L, et al. Suppressing unsteady flow in arteriovenous fistulae. Phys Fluids 2017;29:101901.
[41] Yang C, et al. The anastomotic angle of hemodialysis arteriovenous fistula is associated with flow disturbance at the venous stenosis location on angiography. Front Bioeng Biotechnol 2020;8:846.
[42] Cunnane CV, et al. The presence of helical flow can suppress areas of disturbed shear in parameterised models of an arteriovenous fistula. Int J Numer Method Biomed Eng 2019;35(12):e3259.
[43] Kroon W, Bosboom M, Huberts W, Tordoir J, van de Vosse F. Computational model for estimating the short- and long-term cardiac response to arteriovenous fistula creation for hemodialysis. Med Biol Eng Comput 2012;(50).
[44] Mitchell JRA, Schwartz CJ. Arterial disease. Blackwell Scientific Publications 1965; 17(2):69–71.
[45] Krishnamoorthy M, et al. Hemodynamic wall shear stress profiles influence the magnitude and pattern of stenosis in a pig av fistula. Kidney Int 2008;74(11): 1410–9.
[46] Lehoux S, et al. Molecular mechanisms of the vascular responses to haemodynamic forces. J Intern Med 2006;259(4):381–92.
[47] Roux E, Bougaran P, Dufourcq P, Couffinhal T. Fluid Shear Stress Sensing by the Endothelial Layer. Front Physiol 2020;11:861.
[48] Oprea A, et al. Correlation between preoperative vein and artery diameters and arteriovenous fistula outcome in patients with endstage renal disease. Clujul Med 2018;91(4):399–407.
[49] Gameiro J, Ibeas J. Factors affecting arteriovenous fistula dysfunction: a narrative review. J Vasc Access 2020;21(2):134–47.
[50] Stoumpos S, et al. Ferumoxytol mr angiography versus duplex us for vascular mapping before arteriovenous fistula surgery for hemodialysis. Radiology 2020; 297(1):200069.